Hearing Research 453 (2024) 109127



Contents lists available at ScienceDirect

Hearing Research

journal homepage: www.elsevier.com/locate/heares



Research paper



Influence of the cochlear partition's flexibility on the macro mechanisms in the inner ear

Simon Kersten [a,*,1], Henning Taschke [b], Michael Vorländer [a,2]

[a] Institute for Hearing Technology and Acoustics, RWTH Aachen University, Aachen, Germany
[b] formerly at: Institute of Communication Acoustics, Ruhr University Bochum, Bochum, Germany

ARTICLE INFO

Dataset link: https://doi.org/10.5281/zenodo.13897017

Keywords:
Cochlear partition
Osseous spiral lamina
Cochlear partition bridge
Basilar membrane
Inner ear
Intracochlear pressure
Cochlear impedance

ABSTRACT

Recent studies have highlighted the anatomy of the cochlear partition (CP), revealing insights into the flexible nature of the osseous spiral lamina (OSL) and the existence of a flexible cochlear partition bridge (CPB) between the OSL and the basilar membrane (BM). However, most existing inner ear models treat the OSL as a rigid structure and ignore the CPB, neglecting their potential impact on intracochlear sound pressure and motion of the BM. In this paper, we investigate the effect of the CP's flexibility by including the OSL and CPB as either rigid or flexible structures in a numerical anatomical model of the human inner ear. Our findings demonstrate that the flexibility of the OSL and the presence of the CPB significantly affect cochlear macro mechanisms, including differential intracochlear sound pressure, resistive behavior in cochlear impedances, CP stiffness, and BM velocity. These results emphasize the importance of considering the flexibility of the entire CP to enhance our understanding of cochlear function and to accurately interpret experimental data on inner ear mechanics.

1. Introduction

Recent attention has been drawn to the anatomy of the cochlear partition (CP) and its significance in sound propagation within the human inner ear, particularly focusing on structures such as the cochlear partition bridge (CPB) and the osseous spiral lamina (OSL) (Raufer et al., 2019, 2020; Kerkhofs et al., 2023; Bom Braga et al., 2023). These studies revealed that the OSL comprises two thin, porous structures, known as vestibular and tympanic plates, enveloping soft tissue and the auditory nerves (Raufer et al., 2020; Bom Braga et al., 2023). The CPB, a soft tissue structure, connects the OSL laterally to the basilar membrane (BM). It shares a similar width with the BM (Raufer et al., 2020) and exhibits comparable motion amplitudes (Raufer et al., 2019).

Pioneering experiments by von Békésy (1960), which included measurements of the CP stiffness, already suggested a CP motion not confined solely to the BM but also involving the OSL. Subsequent investigations extended these findings by measuring BM and OSL velocities at locations about 12 mm from cochlear base (Stenfelt et al., 2003) or radial velocity distributions in its vicinity (Raufer et al., 2019). Yet, experimental data on the OSL and the combined CP motion remain scarce and spatially limited.

Overlooking the CP motion related to the OSL's flexibility and the existence of the CPB, the majority of inner ear models treat these as rigid structures [refer to De Paolis et al. (2017) for an overview of models of the hearing system including inner ear models]. Exceptions, such as the work by Taber and Steele (1981), have investigated the effect of the OSL's flexibility. Using a mathematical box model, they revealed that the OSL deflection might predominate the CP motion compared to the BM deflection in the basal region. Building upon this, Kohllöffel (1983) speculated that the flexible OSL could have the effect of shunting the wave propagation in the cochlear fluid, thereby affecting the cochlear input impedance. Indeed, cochlear impedance measurements have indicated resistive characteristics of the cochlear input impedance and the differential impedance across the CP

Abbreviations: CP, cochlear partition; CPB, cochlear partition bridge; OSL, osseous spiral lamina; BM, basilar membrane; OW, oval window; RW, round window; SV, scala vestibuli; ST, scala tympani; SL, spiral ligament; u_r, u_s, radial and longitudinal CP coordinates; p_{sv}, p_{st}, intracochlear pressures in SV and ST; $p_{diff}=p_{sv}-p_{st}$, differential pressure; p_{cp}, CP pressure applied to determine CP stiffness; q_{ow}, q_{rw}, volume velocities at the OW and RW; Z_{diff}, differential impedance across the CP; Z_{rw}, RW impedance; Z_c, cochlear input impedance; v_{cp}, CP velocity; $v_n(\mathbf{x})$, local normal component of the CP velocity at position $\mathbf{x}$; E, Young's modulus; ρ, density; ν, Poisson's ratio; η, structural loss factor; d, thickness; c, speed of sound; G, shear modulus; E_r, E_s, G_{rt}, ν_{rs}, ν_{st}, transversely isotropic material properties of the BM and CPB; d_{bm}, d_{cpb}, BM and CPB thicknesses; ω, angular frequency.

* Corresponding author.
E-mail address: simon.kersten@akustik.rwth-aachen.de (S. Kersten).
[1] ORCID: 0000-0003-3303-9297.
[2] ORCID: 0000-0002-7010-8370.

https://doi.org/10.1016/j.heares.2024.109127
Received 2 July 2024; Received in revised form 18 September 2024; Accepted 30 September 2024
Available online 5 October 2024
0378-5955/© 2024 The Author(s). Published by Elsevier B.V. This is an open access article under the CC BY license (http://creativecommons.org/licenses/by/4.0/).

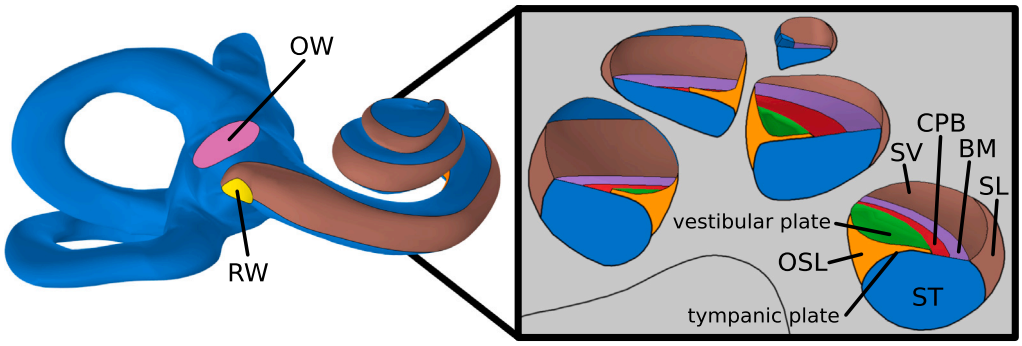

Fig. 1. Geometry of the inner ear model and cross-sectional view through the SV. The vestibule, SV, and ST were considered as fluid domains (blue). The OSL (orange) and SL (brown) were considered as solid domains. Shell physics was assigned to the RW (olive), vestibular and tympanic plates (green), CPB (red), and BM (purple). As the stimulation, an inward velocity was applied at the OW (pink). Refer to Raufer et al. (2020) for views of CPs including cochlear microstructures, which are not contained in detail in our model.

(Aibara et al., 2001; Nakajima et al., 2009; Frear et al., 2018), rather than inertial characteristics which would be associated with cochlear fluid.

This paper aims to enhance the understanding of the cochlear macro mechanisms by investigating the impact of the flexibility of the OSL and CPB using a numerical, anatomical model of the human inner ear. By including the OSL and CPB as either rigid or flexible structures, our model enables a 3D investigation of CP motion and intracochlear sound pressures, elucidating related mechanisms and revealing relations between experimental data on cochlear impedances (Frear et al., 2018), CP stiffness (von Békésy, 1960), and CP motion (Gundersen et al., 1978; Stenfelt et al., 2003; Raufer et al., 2019).

2. Methods

2.1. Finite element model

2.1.1. Geometry

The geometry of the inner ear model, depicted in Fig. 1, includes fluid-filled domains representing the vestibule, semicircular canals, helicotrema, scala vestibuli (SV), and scala tympani (ST). In this model, the scala media is encompassed by the SV, assuming negligible effects from Reissner's membrane, which separates the SV and scala media, consistent with common modeling approaches (e.g., Gan et al., 2007; Kim et al., 2011; Koike et al., 2012; Kim et al., 2014; Stenfelt, 2015; Motallebzadeh et al., 2018; Ren et al., 2021). The CP separates SV and ST, with the CPB and BM boundary surfaces connecting the OSL with the spiral ligament (SL). On the medial side, the OSL domain is bounded by a surface aligned with the innermost part of the SV and ST (refer to Fig. 1). The entire inner ear geometry, except for the oval window (OW) and round window (RW), is embedded in a surrounding block of solid material assigned with fixed boundary conditions (not visible on the left side of Fig. 1, depicted as the gray area in the right panel of the figure). The widths of the BM and CPB each range from approximately 120 μm at the base to around 470 μm at the helicotrema, while the OSL width reaches values of 1000–1300 μm in the basal region and narrows to 250–470 μm near the apex. These values align well with those obtained from histological sections by Raufer et al. (2020, Figure 2 and Table 1). To integrate the material properties and thicknesses of the BM, the CPB, the vestibular plate, and the tympanic plate, shell physics was assigned to these boundaries, allowing for the independent specification of these parameters relative to the adjacent domains.

The inner ear geometry was originally created as part of the work presented in Taschke (2005), using a dataset comprising 75 images from serial sections with a slice thickness of 20 μm, each with a resolution of approximately 40 μm in the image plane and spaced 20–100 μm apart. These images were provided by the Department of Otorhinolaryngology, Head and Neck Surgery at the University Hospital Zürich. Contours of the scalae, vestibule, and semicircular canals were segmented in the slices and reconstructed as non-uniform rational B-spline (NURBS) models, commonly used in computer graphics and computer-aided design (CAD). Adjustments based on literature data were made to regions not fully detailed in the image data and to incorporate more detailed anatomical information published since 2005. These adjustments included refinements at the helicotrema, cochlear base, RW, OSL, and CPB (Gray and Lewis, 1918; Anson and Donaldson, 1981; Cohen et al., 2005; Li et al., 2007; Atturo et al., 2014b,a; Wright and Roland, 2018; Agrawal et al., 2018; Raufer et al., 2019, 2020; Bom Braga et al., 2023). For more detailed information on the model creation procedure, readers are referred to Taschke (2005) for the original methodology.

2.1.2. Material properties

The material properties of the model, along with their respective references, are summarized in Table 1. Soft tissues were assigned a density of 1000 kg/m^3 (Kim et al., 2014) and a Poisson's ratio of 0.45, reflecting their nearly incompressible nature.

The vestibular and tympanic plates were assigned a Young's modulus and density of 8 GPa and 1800 kg/m^3, considering average data for temporal bone presented by Auperrin et al. (2014), and a Poisson's ratio of 0.3. The thickness of the plates (10 μm) was determined based on the anatomical images by Raufer et al. (2020) and Bom Braga et al. (2023). Although the plates are sparsely connected by randomly distributed, small bony pillars (Raufer et al., 2019; Bom Braga et al., 2023), this level of detail was not feasible in the model; instead, a connection of the plates at the lateral edge ensured synchronous motion. For the OSL domain (orange in Fig. 1), a Young's modulus of 30 kPa was assumed to reflect soft tissue properties (Akhmanova et al., 2015), accounting for the tissue and nerve fibers between the two plates (Raufer et al., 2020; Bom Braga et al., 2023).

The mechanical characteristics of the BM and CPB, primarily determined by the radial collagen II fibers (von Békésy, 1960; Liu et al., 2015; Raufer et al., 2020), were represented by the properties of the shell structure. The inhomogeneity, the anisotropy, and the varying thickness were implemented by adjusting the material properties and thickness of the shell along the CP (Gan et al., 2007; Kim et al., 2011, 2014; Koike et al., 2012; Ren et al., 2021) as functions of curvilinear longitudinal and radial coordinates (u_s and u_r), which were obtained by numerically solving differential equations (see Appendix for details). Assuming the radial fibers to be transversely isotropic requires specifying five parameters (Fleischer et al., 2010; Ren et al., 2021). To cover the audible frequency range, the Young's modulus E_r in the direction of the fibers was made a function of distance along the CP (Taschke, 2005; Kim et al., 2011) by utilizing the coordinate u_s (see Fig. A.8(a) for an illustration of u_s). The values of E_r fall within reported ranges for collagen fibers (Heim et al., 2006; Yang et al., 2008). E_s (radial to the fibers' orientation) was set to $E_r/100$, the shear modulus G_{rt} to $E_s/10$, the Poisson's ratios ν_{rs} and ν_{st} to 0.45

Table 1
Material properties assigned to the domains and boundaries in the model. E: Young's modulus, ρ: density, ν: Poisson's ratio, η: structural loss factor, d: thickness, c: speed of sound. The longitudinal and radial CP coordinates u_s and u_r are illustrated in Fig. A.8.

Material	Property	Value		Reference/Explanation
Vestibular and tympanic plates	E	8000	MPa	Auperrin et al. (2014) (temporal bone)
	ρ	1800	kg/m^3	Auperrin et al. (2014) (temporal bone)
	ν	0.3		Chang et al. (2016) (cortical bone)
	η	0.3		Lim et al. (2022) (cortical bone)
	d	10	µm	cf. images in Raufer et al. (2020), Bom Braga et al. (2023)
OSL	E	0.03	MPa	Assumed based on Akhmanova et al. (2015)
	ρ	1000	kg/m^3	
	ν	0.45		
	η	0.5		
BM/CPB	E_r	3500×0.5^{u_s}	MPa	Assumed based on Yang et al. (2008)
	E_s	$E_r/100$		
	G_{rt}	$E_s/10$		
	ν_{rs}, ν_{st}	0.45		
	ρ	1000	kg/m^3	
	η	0.1		
	d_{bm}	$6.3 \times e^{-5.8u_s} + 0.8$	µm	Bhatt et al. (2001) (fit of average data)
	d_{cpb}	$20 - [20 - d_{\mathrm{bm}}(u_s)] \times 2u_r$	µm	cf. images in Raufer et al. (2020)
RW	E	0.2	MPa	Matching Z_{rw} to Frear et al. (2018)
	ρ	1000	kg/m^3	Koike et al. (2012), Ren et al. (2018)
	ν	0.45		
	η	0.3		Matching Z_{rw} to Frear et al. (2018)
	d	70	µm	Goycoolea and Lundman (1997)
SL	E	E_r		
	ρ	1000	kg/m^3	
	ν	0.45		
	η	0.5		
Cochlear fluid	c	1500	m/s	Kim et al. (2011)
	ρ	1000	kg/m^3	Kim et al. (2011)

(similar to Fleischer et al., 2010), and the isotropic loss factor to 0.1. BM and CPB width were approximately equal (Raufer et al., 2020). Given spatially sparse data on the BM thickness (Bhatt et al., 2001; Liu et al., 2015; Meenderink et al., 2019), approximations were made based on values from Bhatt et al. (2001). CPB thickness was set to linearly increase from the BM thickness at the CPB–BM edge to 20 µm at the OSL–CPB junction. The thickness functions are given in Table 1. As it will be shown in Section 3, these parameters yielded plausible traveling wave propagation and tonotopic mapping (Greenwood, 1990), and BM velocities similar to measured curves (Stenfelt et al., 2003; Raufer et al., 2019).

At the lateral side of the CP, the BM fibers fan out into the SL (Raufer et al., 2020), therefore the BM's radial Young's modulus E_r was assigned to the SL. The RW membrane thickness was set to 70 µm (Goycoolea and Lundman, 1997), with its properties determined to match experimental impedance data (Frear et al., 2018). The cochlear fluid was modeled as incompressible with water-like properties (Kim et al., 2011).

To evaluate the impact of the OSL and CPB flexibility, either the OSL alone or both the OSL and CPB were rendered rigid by applying fixed boundary conditions to these structures in subsets of the simulations.

Active cochlear mechanisms (Dallos, 1992; Robles and Ruggero, 2001) and fluid viscosity, which has been shown to influence these active mechanisms and cochlear micromechanics (Wang et al., 2016; Motallebzadeh and Puria, 2021), were not accounted for. However, since our results are compared with experimental data obtained from human cadaver ears, a linear modeling approach is considered appropriate. Additionally, this study focuses on cochlear macromechanics, with microstructures associated with the BM and CPB effectively represented using shell physics. Consequently, the assigned loss factors (Table 1) should be interpreted as encompassing losses both in the fluid near the BM and CPB and within these structures themselves.

2.1.3. Stimulation and boundary conditions

A unit inward velocity was applied to the OW, approximating a piston motion of the stapes. An exception was the determination of the stiffness of the CP, where a uniform sound pressure of 1 Pa at a frequency of 1 Hz was applied to the CP surfaces from the ST side. The pressure acoustics physics was deactivated in the model in this case, removing the load imposed by the fluid. This is equivalent to applying a uniform differential pressure across the CP, allowing for CP motion to be determined by its structural properties only. The frequency of 1 Hz was chosen to ensure excitation far below the resonance frequencies of the BM to obtain stiffness.

2.1.4. Simulation parameters and post-processing

The simulations were conducted using Comsol Multiphysics® version 6.2, covering frequencies from 100 Hz to 10 kHz with a resolution of 24 frequencies per octave. Utilizing the software's default quadratic shape functions, we set the maximum element size of the triangular mesh on the BM/CPB boundary to 40 µm. The maximum element size of the remaining tetrahedral mesh was adjusted to ensure at least 5 elements per wavelength for 10 kHz, considering the bending wave speed on the shell boundaries, shear wave speed in the solid domains, and the speed of sound in the fluid domain. The mesh was kept the same for all frequencies. The total number of degrees of freedom for the full model with flexible OSL and CPB was approximately 3.2 million, the number was slightly reduced when these structures were considered fixed. Evaluation quantities (see Section 2.2) were exported in .csv format and analyzed using custom Python scripts. The finite element model, simulation results, and Python code used for the analysis are provided at https://doi.org/10.5281/zenodo.13897017.

2.2. Evaluation quantities

Following experimental setups, such as those by Olson (1998), Nakajima et al. (2009) and Frear et al. (2018), intracochlear sound pressures p_{sv} and p_{st} were assessed using virtual sound probes at the corresponding locations in the SV and the ST, respectively. The differential sound pressure was then computed as $p_{\mathrm{diff}} = p_{\mathrm{sv}} - p_{\mathrm{st}}$ (Nakajima et al., 2009; Frear et al., 2018). Volume velocities q_{ow} and q_{rw} were determined by integrating the normal component of the acoustic particle velocity over

the OW and RW boundaries, respectively. The impedance definitions followed Frear et al. (2018),

$$Z_{\mathrm{diff}} = p_{\mathrm{diff}}/q_{\mathrm{ow}}\,, \tag{1}$$

$$Z_{\mathrm{rw}} = p_{\mathrm{st}}/q_{\mathrm{ow}}\,, \tag{2}$$

$$Z_{\mathrm{c}} = p_{\mathrm{sv}}/q_{\mathrm{ow}} = Z_{\mathrm{diff}} + Z_{\mathrm{rw}}\,. \tag{3}$$

These definitions assumed $q_{\mathrm{ow}} \approx q_{\mathrm{rw}}$ and were evaluated similarly to facilitate comparison with experimental data, except for the method for obtaining q_{ow} and q_{rw}.

The CP velocity v_{cp} was assessed at the ST boundary of the CP (Stenfelt et al., 2003; Raufer et al., 2019). Specifically, longitudinal velocity distributions were evaluated via linear interpolation of the simulation results at the radial BM center ($u_r = 0.75$) and the OSL–CPB junction ($u_r = 0$). Additionally, radial velocity profiles were examined at relative longitudinal distances of 0.03 and 0.3, which correspond to locations with available experimental data (Stenfelt et al., 2003; Raufer et al., 2019), as well as at an additional position closer to the apex at 0.7 relative distance. The differential velocity between the BM center and OSL–CPB junction was assessed as the component-by-component difference between the velocity vectors at the same longitudinal distances u_s. The three complex-valued components of the CP and differential velocity vectors were condensed into single quantities by calculating the magnitude and phase of their maximum per unit cycle (Dobrev and Sim, 2018).

Velocities were normalized to p_{diff}, viewed as the pressure initiating the traveling wave, or q_{ow}, regarded as the cochlear input, to enable comparison with experimental data (Gundersen et al., 1978; Stenfelt et al., 2003; Raufer et al., 2019).

CP stiffness was calculated as $-\omega\,\mathrm{Im}(p_{\mathrm{cp}}/v_{\mathrm{n}}(\mathbf{x}))$ for the corresponding stimulation with a homogeneous pressure $p_{\mathrm{cp}} = 1\,\mathrm{Pa}$ on the ST side of the CP at $\omega = 2\pi \times 1\,\mathrm{Hz}$. $v_{\mathrm{n}}(\mathbf{x})$ represents the local normal component of the structural velocity in the direction of the load at a position $\mathbf{x}$ on the CP.

Given the specific geometry and set of material properties, it is important to consider that the numerical model used in this study should be viewed as representative of an individual specimen rather than a predictive model for average data when comparing the simulation results to experimental data in the following.

3. Results

3.1. Cochlear impedances

In Fig. 2, cochlear impedance results are shown for the three conditions: flexible OSL and CPB (solid lines), rigid OSL and CPB (dashed lines), and rigid OSL alone (dash-dotted lines). These results are compared to experimental data from Frear et al. (2018) (individual data and mean for Z_{diff} and Z_{rw}), Aibara et al. (2001) (mean ± standard deviation for Z_{c}), and Nakajima et al. (2009) (mean ± standard deviation for Z_{c}).

Z_{diff} (left column) displays inertia-dominated behavior up to approximately 4 kHz for the rigid OSL and CPB condition (dashed line) and up to 3 kHz for the rigid OSL alone (dash-dotted line). Below 3 kHz, the curves are similar for both conditions. In both cases, the magnitude of Z_{diff} exceeds the experimental data between 800 Hz and 4 kHz. Experimental investigations have revealed that, on average, Z_{diff} exhibits resistive behavior with an additional inertial component at low frequencies (Frear et al., 2018). However, unlike a pure resistance, both the magnitude and phase of individual measured impedances vary with frequency (cf. Nakajima et al., 2009; Frear et al., 2018). These characteristics observed in individual experimental data are replicated with flexible OSL and CPB (solid line), where Z_{diff} shows frequency-dependent variability in magnitude within a range of 15 dB and a phase alternating around zero with a tendency towards positive values at the lowest frequencies.

At frequencies below approximately 400 Hz, Z_{diff} exhibits similar behavior across all three conditions. However, between 400 Hz and 500 Hz, the presence of a zero crossing in the phase and a change in the slope of the magnitude with flexible OSL and CPB indicates a mass–spring resonance. The absence of this resonance in the two scenarios with rigid OSL suggests that it is primarily driven by the flexibility of the OSL rather than the CPB. At around 1.5 kHz, Z_{diff} undergoes another characteristic change, leading to a minimum in magnitude. This phenomenon is linked to a shift in the radial motion of the OSL at the base, as discussed in Section 3.3.2.

Z_{rw} in Fig. 2(b) resembles the experimental data, demonstrating the behavior of a spring–mass resonator (Frear et al., 2018). Above approximately 2 kHz, the variation in magnitude and phase among the individual experimental data becomes more pronounced. While positive phase values are observed with a rigid OSL and CPB, introducing flexibility to the OSL results in negative phase values. Notably, all three curves remain within the range of the experimental data.

The cochlear input impedance Z_{c} [Fig. 2(c)] is essentially a series connection of Z_{diff} and Z_{rw} [(a) and (b), respectively]. Since Z_{c} is primarily dominated by Z_{diff}, the differences between the flexible and rigid CP conditions correspond to those observed for Z_{diff}. With flexible OSL and CPB (solid line), Z_{c} generally aligns with the range of the experimental data reported by Aibara et al. (2001) and Nakajima et al. (2009). In contrast, for the two conditions with rigid OSL, the importance of the cochlear fluid is predicted to be high, as indicated by the phase being close to $\pi/2$ and the magnitude exceeding the experimental data range, particularly above 500 Hz.

3.2. CP stiffness

Fig. 3 shows the stiffness of the CP obtained by applying a uniform pressure on the CP at a frequency of 1 Hz while evaluating the normal velocity at the radial center of the BM. The results are shown with flexible OSL and CPB (solid black line), rigid OSL and rigid CPB (dashed black line), and rigid OSL with flexible CPB (dash-dotted black line).

For comparison, the CP stiffness at the OSL–CPB junction with flexible OSL is depicted in orange. Unlike the BM and CPB, the OSL does not react purely locally to the uniform pressure. Instead, it sometimes exhibits a lever-like motion, resulting in velocity in the opposite direction of the load for relative distances around 0.8, leading to non-meaningful stiffness values. Consequently, Fig. 3 presents stiffness values at the OSL–CPB junction only where physically meaningful results were obtained under the pressure load. Note that for the scenarios with rigid OSL, the stiffness at this junction approaches infinity.

With both the OSL and CPB rigid (dashed line), the stiffness at the center of the BM is governed solely by the stiffness of the BM itself. Introducing the CPB as a flexible structure slightly reduces this stiffness at the BM center across all distances (dash-dotted line). In both scenarios, the stiffness gradually decreases from the base to the apex due to the increasing width and decreasing Young's modulus of the BM/CPB section, along with the decreasing BM thickness (see Section 2).

Interestingly, the flexibility of the OSL does not significantly influence BM stiffness beyond positions apical to a relative distance of approximately 0.3 along the CP (cf. black solid and dash-dotted lines). However, noticeable differences emerge in the basal region, where BM stiffness (solid black line) resembles the stiffness at the lateral edge of the OSL (orange line). This suggests that in this region, CP stiffness is primarily influenced by the flexibility of the OSL rather than the properties of the BM and CPB.

With flexible OSL and CPB, CP stiffness predominantly falls within the range of $1{\times}10^6$–$5{\times}10^8$ Pa/m. This aligns reasonably well with the range of $4{\times}10^6$–$1{\times}10^8$ Pa/m reported by Olson et al. (2012), derived from human cochlear data at nine CP positions from von Békésy (1960). In contrast, for the conditions with rigid OSL, CP stiffness near the base reaches significantly higher values than those observed with flexible OSL.

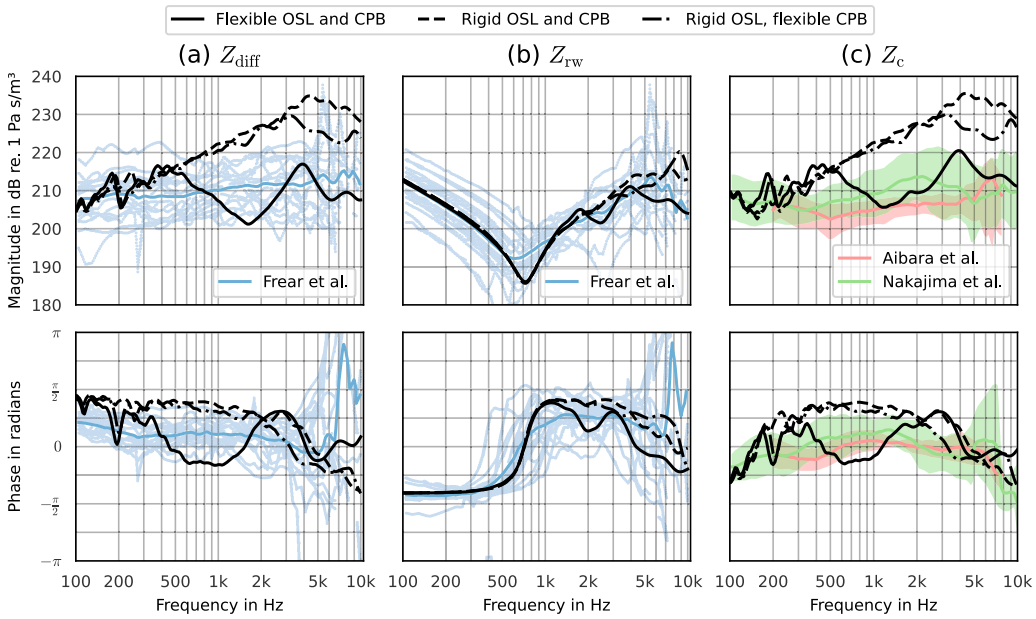

Fig. 2. Magnitude and phase of cochlear impedances with flexible versus rigid OSL and CPB. For comparison, mean and individual data from Frear et al. (2018) are shown for Z_{diff} and Z_{rw}. Z_c is compared to experimental data by Aibara et al. (2001) and Nakajima et al. (2009) (mean ± standard deviation).

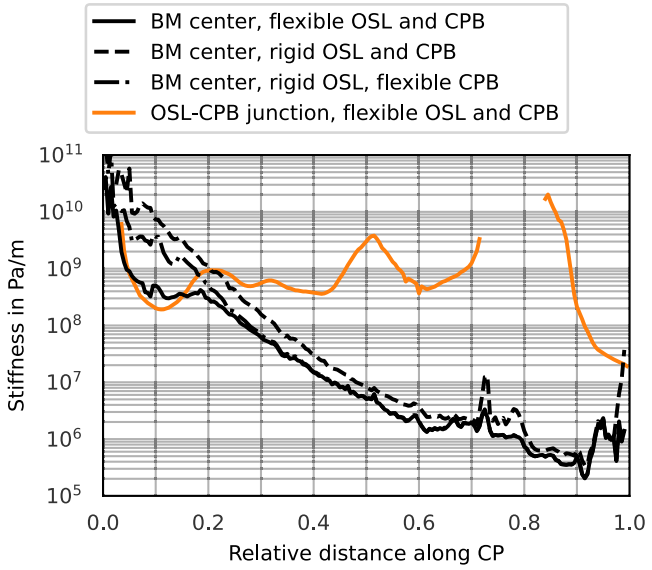

Fig. 3. CP stiffness evaluated at radial BM center with flexible OSL and CPB (solid black line), rigid OSL and rigid CPB (dashed black line), and rigid OSL/flexible CPB (dash-dotted black line) along the CP. For comparison, the stiffness at the OSL–CPB junction with flexible OSL and CPB is shown in orange (note that it approaches infinity for the scenarios with rigid OSL).

3.3. CP motion

3.3.1. Velocity at specific positions

Fig. 4 depicts the magnitude and phase of the CP velocity v_{cp} evaluated at the radial center of the BM (black) and OSL–CPB-junction (orange), normalized to the differential intracochlear pressure p_{diff} [(a)–(c)] and to the OW volume velocity q_{ow} [(d)–(f)] at relative distances of 0.03, 0.3, and 0.7 along the CP.

Raufer et al. (2019) presented CP velocity data close to the cochlear base for several radial positions normalized to the sound pressure in the vestibule. As the sound pressure in the SV (p_{sv}) exceeds that in the ST (p_{st}) at most frequencies ($Z_c > Z_{rw}$ in Fig. 2), their data can be compared to the simulation results regarding v_{cp}/p_{diff}. The blue line in Fig. 4(a) represents their data at the radial center of the BM (specimen #16), with their position of 1 mm from the base corresponding to a relative distance of about 0.03. The sign of the phase was adjusted, so that a positive v_{cp} refers to a motion in the direction from SV to ST following our definition of p_{diff} (refer to Section 2.2).

The results with flexible OSL and CPB (solid black line) are in reasonable agreement with the experimental data at this position (blue), particularly when considering the sensitivity of velocity magnitude to slight variations in both radial and longitudinal directions near the base (see Sections 3.3.2 and 3.3.3 for details). The magnitude of the velocity consistently increases across the inspected frequency range, with slopes of approximately 20 dB per decade below 1 kHz and above 1.5 kHz. This increase suggests that the characteristic frequency for this position is above the maximum inspected frequency of 10 kHz, consistent with Raufer et al. (2019), who reported characteristic frequencies between 9.5–14.4 kHz for this location in six temporal bone specimens. The curve with a rigid OSL and a flexible CPB (dash-dotted) is about 5 dB lower than the curve with flexible OSL and CPB below 1 kHz, and 15–20 dB lower above 1.5 kHz. This curve is about 15 dB higher than the curve with both rigid OSL and rigid CPB (dashed). Both curves with a rigid OSL show a constant slope with an increase of 20 dB per decade. The velocity at the junction of the flexible OSL with the CPB (orange) is nearly equal in magnitude to the velocity at the BM center for this condition below 1 kHz and about 5 dB lower above 1.5 kHz.

The nearly constant phase of about $-\pi/2$ in the experimental and simulation results at the BM center (black and blue lines) indicate a spring-like behavior at this position within the inspected frequency range. The phase difference of about π between the BM center and OSL–CPB junction above about 1 kHz indicates a change in radial motion with frequency at this position (see Section 3.3.2).

At a relative distance of 0.3 in Fig. 4(b), the magnitude curves for the rigid OSL (dashed and dash-dotted black lines) display a nearly constant slope of 20 dB per decade, increasing steadily before reaching peaks at approximately 5 kHz and 3 kHz, respectively, followed by a sharp decline. With a flexible OSL (solid black line), the magnitude exhibits a similar overall pattern, though with a slightly steeper increase between about 400 Hz and 1.5 kHz, a section of highest magnitude between 1.5–3 kHz, and an additional local maximum around 6.5 kHz approximately 10 dB below the overall maximum. The magnitude of

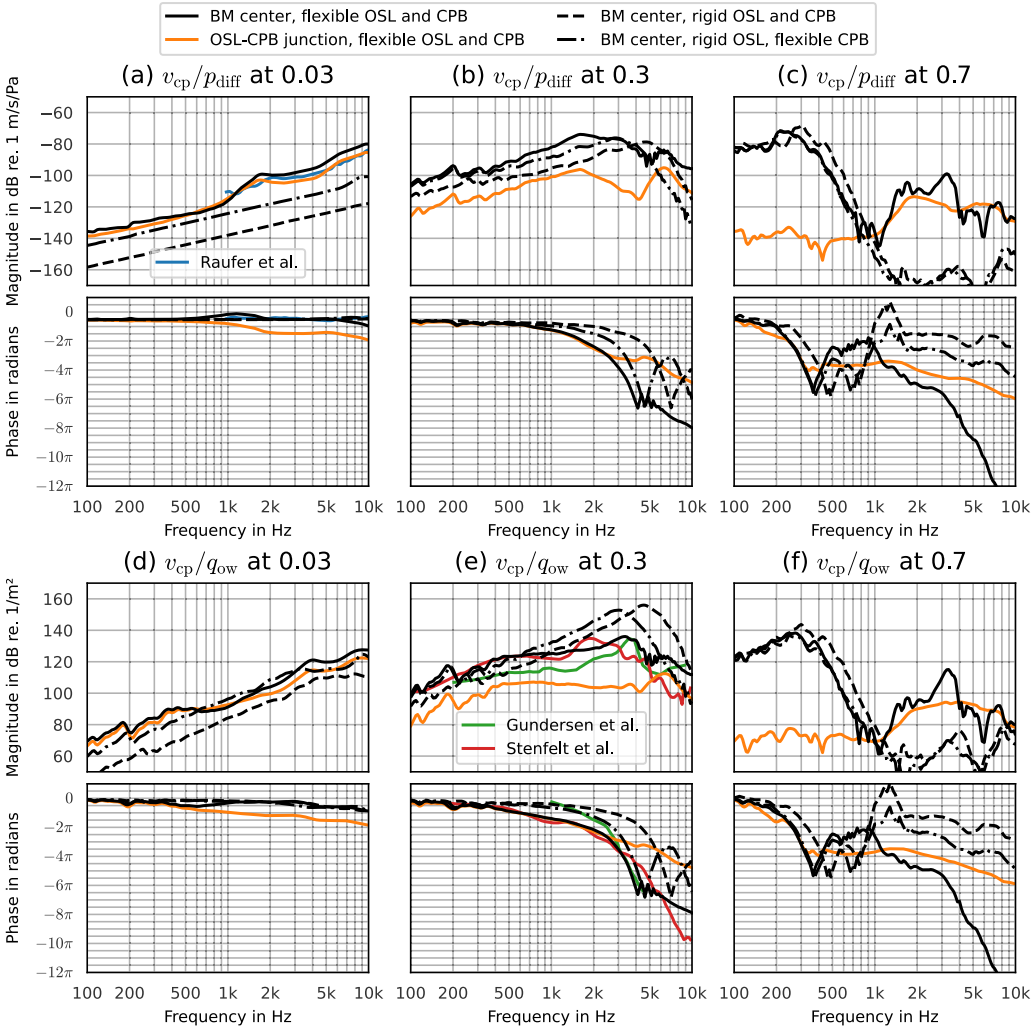

Fig. 4. CP velocity v_{cp} normalized to differential cochlear pressure p_{diff} (top row), and OW volume velocity q_{ow} (bottom row) evaluated at relative distances of 0.03 (left), 0.3 (center), and 0.7 (right) along the CP. Solid black lines indicate results with a flexible OSL and CPB, dashed black lines with a rigid OSL and rigid CPB, and dash-dotted black lines with a rigid OSL and flexible CPB, each evaluated at the radial BM center. Solid orange lines indicate the velocity at the OSL–CPB junction with a flexible OSL (note that it equals zero in the scenarios with rigid OSL). The experimental data from Raufer et al. (2019) in (a) was measured close to the base at the radial center of the BM. The data from Gundersen et al. (1978) and Stenfelt et al. (2003) at a distance 12 mm from base (corresponds to approximately 0.3 relative distance in the model) in (e) was recalculated following the method in Frear et al. (2018).

the velocity at the OSL–CPB junction (solid orange line) shows an alternating slope with frequency, characterized by an increase below approximately 1.5 kHz and within the 4–6 kHz range, and a decrease in between and above these ranges.

For all three conditions, the rapid decrease in phase, particularly above 1 kHz, indicates traveling wave propagation in the BM (Zweig et al., 1976) and at the OSL edge (Stenfelt et al., 2003). Comparing the phase response between the three scenarios, the lowest phase lag is achieved with both rigid OSL and rigid CPB. Including these structures as flexible each increases the phase lag. Compared to the radial BM center, the phase lag at the OSL–CPB junction (orange) is similar below the characteristic frequency, while the curves differ by about 4π above. In the two conditions with a rigid OSL, partial phase increases in phase are observed above approximately 4.5 kHz and 7 kHz. These increases result from the phase being too steep to be unwrapped accurately, given the frequency resolution of the simulation in this range.

At a relative distance of 0.7 in Fig. 4(c), the maximum magnitudes in BM velocity (black lines) are reached between 200–300 Hz, with an increase at lower frequencies and a sharp decrease above. When both the OSL and CPB are rigid (dashed line), the maximum shifts slightly towards higher frequencies compared to the conditions with a flexible CPB. Accompanied by a decrease in phase up to approximately 400 Hz, these characteristics indicate the presence of a BM traveling wave in all three conditions. A distinct influence of the OSL becomes evident above 1 kHz, where its flexibility results in BM velocities 40 dB higher compared to the other two conditions. In this frequency range, the velocities at BM center and OSL–CPB junction (orange line) show similar curve shapes, while the velocity at the OSL edge remains approximately 60 dB below the BM velocity at low frequencies.

Between approximately 400–500 Hz and 1–2 kHz, the steepness of the phase data at the BM center causes inaccuracies in phase unwrapping for all three conditions. Above 2 kHz, with rigid OSL (dashed and dash-dotted black lines), the reduction in slope of the phase indicates a complete decay of the BM traveling wave (Zweig et al., 1976), corresponding to the magnitude fluctuating around 100 dB below the maxima. In contrast, the decrease in phase at both the BM center (solid black line) and OSL edge (orange line) in this frequency range indicates that traveling-wave behavior within the OSL significantly contributes to BM motion. Additionally, the phase difference between the positions is related to complex radial velocity patterns, inspected in more detail in Section 3.3.2.

While Fig. 4(a)–(c) show the ratio v_{cp}/p_{diff}, normalizing to the differential pressure that initiates the traveling wave, (d)–(f) depict the ratio v_{cp}/q_{ow}, where the CP velocity is divided by the OW volume

velocity, considered as the cochlear input. This is equivalent to multiplying v_{cp}/p_{diff} by Z_{diff}. Consequently, the results in panels (d)–(f) not only reflect the CP velocities shown in (a)–(c) but also incorporate the frequency-dependent effects of the OSL and CPB flexibilities already present in Z_{diff}.

For comparison, experimental BM velocity data from Gundersen et al. (1978) and Stenfelt et al. (2003) at a distance 12 mm from base are included in Fig. 4(e). This data was normalized to OW volume velocity by multiplying the stapes velocity by a factor of 3.22 mm^2 based on the approach in Aibara et al. (2001), Nakajima et al. (2009), Frear et al. (2018). Similar curves in magnitude and phase were observed with flexible OSL and CPB (solid black line) at the relative distance of 0.3, which approximately matches their position.

With a rigid OSL (dashed and dash-dotted black lines), the magnitudes increase with frequency at a slope of 40 dB per decade, reaching maxima at the same frequencies as in panel (b). This increase results from the combined 20 dB slopes of the curves in panel (b) and Z_{diff}. Below 500 Hz, the magnitudes are similar between the three simulation conditions. However, with flexible OSL and CPB (solid black line), as well as in the experimental data (green and red), the magnitudes exhibit a nearly constant section between the initial at low-frequency rise and a second increase towards the maxima between 3 kHz and 4 kHz, respectively, before sharply decreasing. By comparing the simulation results with the differential impedance in Fig. 2(a) and the CP velocity normalized to the differential pressure in Fig. 4(b), it is evident that the constant slope and the maximum observed between 3–4 kHz result from the characteristics of Z_{diff}, which combine with the traveling-wave characteristics evident in the BM velocity in Fig. 4(b). Particularly, the maximum in Fig. 4(e) corresponds closely to the peak at approximately 3.5 kHz in Z_{diff} seen in Fig. 2(a). The magnitude of the velocity at the OSL–CPB junction (solid orange line) is approximately 10 dB below the velocity at the BM center, following a similar slope except around the peak in BM velocity. Consistent with the phase of Z_{diff} remaining within $\pm\pi/2$ [Fig. 2(a)], the phase data in panel (e) mostly follows the phase of (b), indicating traveling wave propagation in both the BM and at the OSL edge (Stenfelt et al., 2003).

At a relative distance of 0.03 in Fig. 4(d), the influence of Z_{diff} results in a nearly constant slope in the magnitude of the BM velocity with flexible OSL and CPB (solid black line) between 400 Hz and 1 kHz. The magnitudes are approximately 5 dB higher than those with rigid OSL and flexible CPB (dash-dotted black line) below 500 Hz, and similar above this frequency. Since Z_{diff} is similar for the two conditions with rigid OSL below 3 kHz [Fig. 2(a)], the 15 dB difference between the corresponding curves in Fig. 4(d) is consistent with (a) in this frequency range, reducing to less than 10 dB at higher frequencies. At a relative distance of 0.7 in Fig. 4(f), the curve characteristics remain consistent with those in Fig. 4(c).

Following the results for v_{cp}/p_{diff} in Fig. 4(a)–(c), the curves in (d)–(f) indicate the presence of traveling wave in both the BM and OSL (Stenfelt et al., 2003), highlighting that the impact of the OSL and CPB varies with frequency and distance along the CP, as further explored in Section 3.3.3.

3.3.2. Radial velocity profiles

The CP velocity results from Fig. 4 at relative distances of 0.03 (left column), 0.3 (center column), and 0.7 (right column) from the base are extended in Fig. 5, which shows radial profiles of the velocity for the condition with flexible OSL and CPB. The radial locations where the velocities were evaluated in Fig. 4 are indicated by vertical black (BM center) and orange lines (OSL–CPB junction). The dotted lines depict the CPB–BM connection. Panels (a)–(c) show the magnitudes of v_{cp} normalized to the differential cochlear pressure p_{diff}, and panels (g)–(i) normalized to the maximum per frequency. Panels (d)–(f) and (k)–(l) illustrate these velocity profiles color-coded, respectively, with frequencies indicated along the y-axis.

Consistent with Fig. 4, changes in magnitude with frequency are evident as horizontal variations at the radial BM center (solid black vertical line) for all three longitudinal positions in Fig. 5(a)–(c). At a relative distance of 0.03, the velocity magnitudes of the OSL, CPB and BM in (a) and (d) generally increase with frequency, however at different rates, leading to variations in velocity profiles with frequency. At higher frequencies [red shades in (a) and (g)], the simulation results show the maxima close to the CPB–BM junction. The velocity at the OSL–CPB junction (orange vertical line) stays 6–10 dB below the maximum in this frequency range. These results align with experimental observations by Raufer et al. (2019, Fig. 2), which were limited to frequencies of 784 Hz and above. Conversely, at lower frequencies [blue shades in (a) and (g)], the OSL portion of the CP exhibits bending with the maximum velocity occurring in the center of the OSL rather than near the CPB. These maxima reach the same velocity magnitudes as those at the BM. Indeed, the measured motions for some of the specimens reported in the supplementary material of Raufer et al. (2019, e.g., Fig. S3 B and F) show a similar characteristic at lower frequencies. The velocities normalized to the maximum per frequency in panels (g) and (j) indicate that the similarity in magnitude between the OSL and BM/CPB section persists up to about 1.5 kHz, coinciding with the characteristic change in Z_{diff} at this frequency [Fig. 2(a)]. Above this frequency, the maximum of the radial velocity distribution is reached at the BM–CPB junction.

The situation differs further from the cochlear base. Panels (k) and (l) indicate characteristic changes in the velocity profiles for relative distances of 0.3 and 0.7 between 6–7 kHz and 800–900 Hz, respectively, above the characteristic frequencies for these positions (cf. Fig. 4). Below these frequencies, some degree of bending is still observed in the OSL at 0.3 relative distance in (h) and (k), particularly in its section close to the CPB, though the radial maximum velocity is reached at the BM. At 0.7 relative distance in (f), the maxima in OSL velocity are more than 25 dB lower than those at the BM. In Fig. 4(b) and (c), the decay of the BM traveling wave is visible above the characteristic frequencies, indicated by a sharp decrease in BM velocity with increasing frequency. This decay results in similar velocity magnitudes across the OSL, CPB, and BM, as shown in the upper parts of Fig. 5(k) and (l). At a relative distance of 0.7, this decay is further accompanied by a radial break-up of the BM/CPB section into a pattern with several maxima instead of a single one. Fig. 5(c) and (f) show that the decay also coincides with an increased motion across the OSL above approximately 1.5 kHz, as already observed at the OSL–CPB junction in Fig. 4(c) and (f).

3.3.3. Longitudinal velocity distributions

The CP velocity results in Figs. 4 and 5 are restricted to specific relative distances of 0.03, 0.3 and 0.7 along the CP. To provide a more comprehensive view, Fig. 6 presents the CP velocity at the radial BM center normalized to p_{diff} in terms of its color-coded magnitude across frequency (x-axes) and along the CP (y-axes) for the three conditions with flexible OSL and CPB (left), rigid OSL and CPB (center), and rigid OSL with flexible CPB (right). The results from Fig. 4(a)–(c) reappear in this representation as horizontal profiles at the corresponding frequencies. For additional context, the tonotopic map after Greenwood (1990) is included. The region left and below the Greenwood curve is characterized by BM traveling wave motion, which decays in the region above and to the right of the curve.

With rigid OSL in Fig. 6(b) and (c), the predominantly diagonal color gradient illustrates the increasing envelope of the BM traveling wave over frequency and distance, reaching a maximum before sharply decreasing. Dark colors in the upper right part of these panels signify the decay of the traveling wave, consistent with observations from Fig. 4 under these conditions.

In contrast, Fig. 6(a) shows that the flexibility of the OSL results in a significant increase in BM motion in the upper right part of the plot, coinciding with the decay of the traveling wave, and also evident in Fig. 4(c) and (f). Furthermore, comparing (a) with (b) and (c) reveals

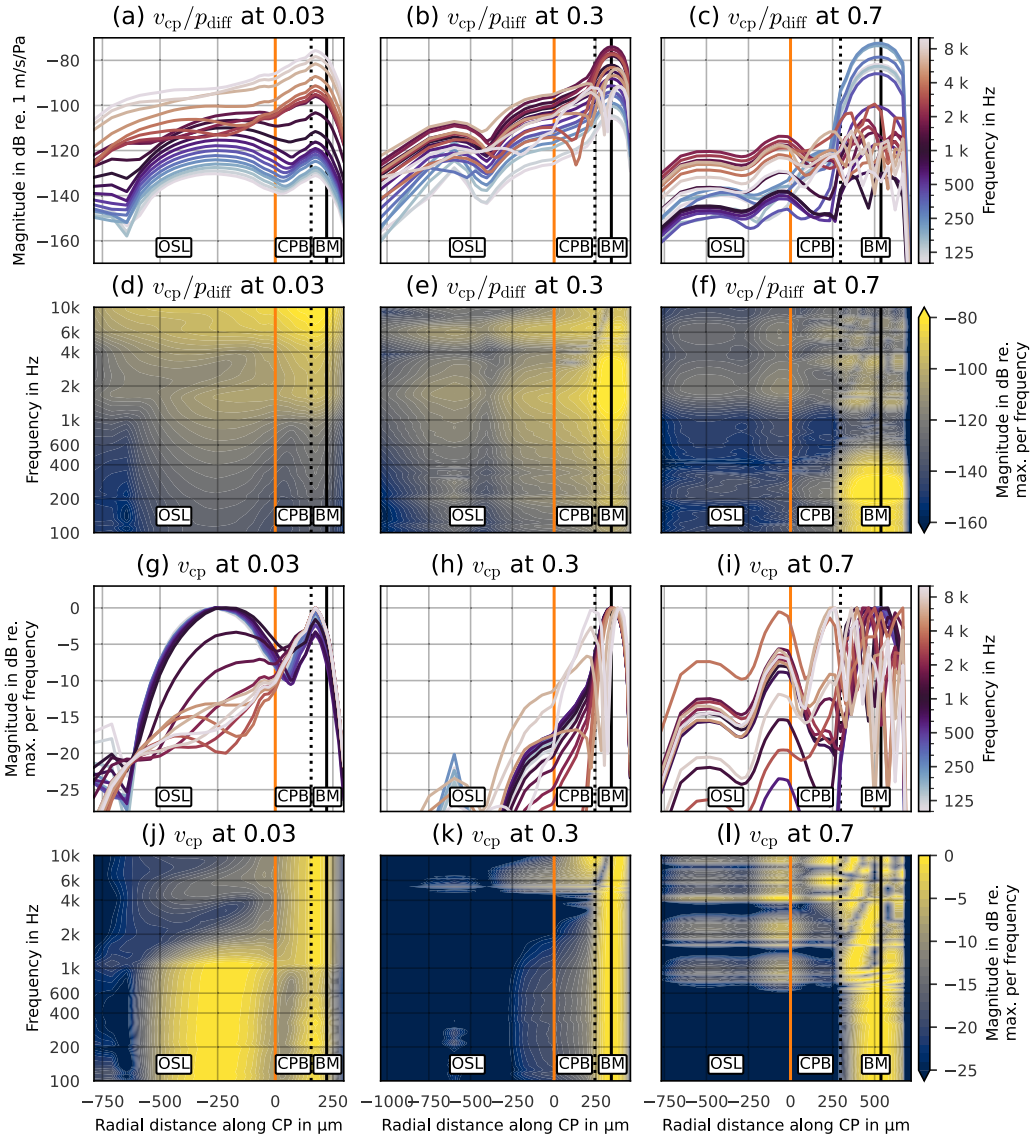

Fig. 5. Profiles of CP velocity v_{cp} with flexible OSL and CPB along radial locations (x-axis), evaluated at relative longitudinal distances of 0.03 (left column), 0.3 (center column), and 0.7 (right column). The vertical black solid lines indicate the BM center, and the orange lines indicate the OSL–CPB junction, corresponding to the radial positions in Fig. 4. The dotted black lines indicate the CPB–BM connection. Panels (a)–(c) depict the magnitudes of v_{cp} normalized to the differential cochlear pressure p_{diff} from 100 Hz to 10 kHz (bright blue to bright red, with 1 kHz in black). Panels (d)–(f) display v_{cp}/p_{diff} in terms of the color-coded magnitude, with frequencies indicated on the y-axis. Panels (g)–(i) and (j)–(l) show the magnitudes of v_{cp} normalized to the maximum per frequency, following the same formats as panels (a)–(c) and (j)–(l), respectively.

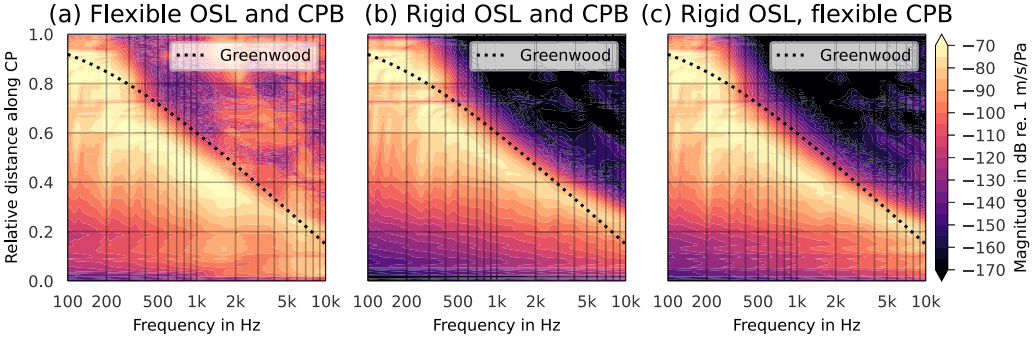

Fig. 6. Magnitude of CP velocity at the radial BM center normalized to differential cochlear pressure p_{diff} with flexible OSL and CPB (left), rigid OSL and CPB (center), and rigid OSL/flexible CPB over frequency (x-axes) and relative distance along the CP (y-axes). The tonotopic map after Greenwood (1990) is provided for reference.

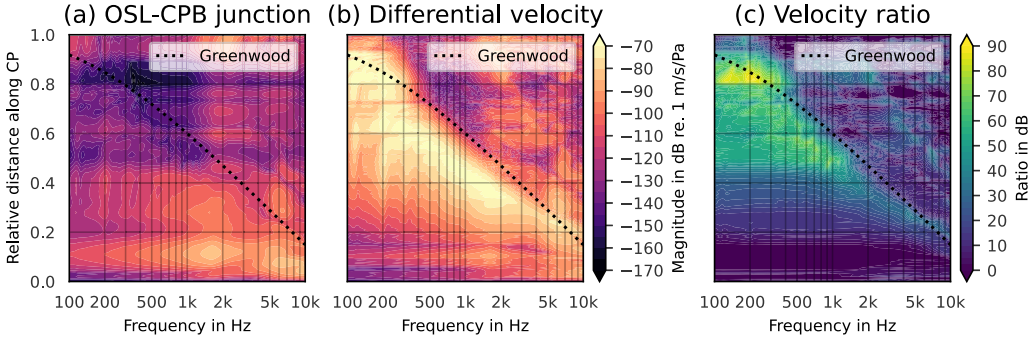

Fig. 7. (a) CP velocity at the OSL–CPB junction and (b) differential velocity between BM center and OSL–CPB junction, both normalized to the differential pressure p_{diff} over frequency (x-axes) and relative longitudinal distance along the CP (y-axes). These results are given for the condition with flexible OSL and CPB. The color ranges correspond to those in Fig. 6. In (c), the ratio of the velocity at the BM center to the velocity at the OSL–CPB junction is illustrated. The tonotopic map after Greenwood (1990) is provided for reference.

that the flexibility of the OSL generally leads to higher magnitudes for relative distances smaller than 0.3, while similar traveling wave magnitudes are reached at positions towards the apex. This trend aligns with differences observed in CP stiffness under the different scenarios, as shown in Fig. 3 (black lines).

Instead of evaluating the velocity at the radial BM center, Fig. 7(a) depicts the longitudinal velocity distribution at the OSL–CPB junction in the same representation as Fig. 6 for the condition with flexible OSL. Comparing Fig. 7(a) with Fig. 6(a), similarities are evident in the lower part of the panels for relative distances below approximately 0.3, which corresponds to similar stiffness in this CP region at these radial locations (Fig. 3). Fig. 7(b) displays the differential velocity between the BM center and the OSL–CPB junction, normalized to the differential pressure. Unlike (a), the diagonal color gradient around the characteristic frequencies indicates a traveling wave in the BM/CPB section of the CP that propagates along the OSL.

To compare BM and OSL velocities, Fig. 7(c) presents the magnitude of the ratio of the velocity at the BM center to the velocity at the OSL–CPB junction. Up to approximately 0.3 relative distance along the CP, the dark blue colors denote similar magnitudes in BM motion compared to CP motion at the OSL–CPB junction, a phenomenon primarily dependent on position and largely independent of frequency within the traveling wave region. Towards the apex and below the characteristic frequencies, the velocity at the BM center associated with the traveling wave progressively surpasses that at the OSL–CPB junction by up to 90 dB at maximum, as depicted by the vertical shift towards yellow colors in Fig. 7(c). This difference again corresponds to the position-dependent difference in CP stiffness in Fig. 3 (black solid vs. orange solid line).

4. Discussion

The numerical model used in this study should be regarded more as representative of an individual specimen rather than a predictive model for average data. Its primary objective is to qualitatively assess mechanisms associated with the flexibility of the CP and to highlight their fundamental implications. Consequently, the magnitudes of these mechanisms and related quantities, such as transition frequencies, will naturally vary among individual ears, as evidenced by the variability in experimental data [see, e.g., Merchant et al., 1996; Puria et al., 1997; Aibara et al., 2001; Puria, 2003; Nakajima et al., 2009; Frear et al., 2018 for cochlear impedances, Raufer et al. (2019, supplementary material) for radial CP motion]. Nevertheless, the simulations presented in this paper have enabled the identification of distinct phenomena related to the flexibility of the CP. These phenomena contribute to the understanding of cochlear impedances, CP stiffness, and the longitudinal and radial distribution of CP motion.

4.1. Cochlear impedances

4.1.1. Differential impedance

In their study, Frear et al. (2018) utilized experimental intracochlear pressure data from multiple specimens to deduce a lumped element model of the differential impedances across the CP, Z_{diff}, incorporating a resistor representing "the wave impedance of the CP and surrounding fluid" (Frear et al., 2018) in parallel to an inductance representing the cochlear fluid at the apex. However, when considering typical material properties for the cochlear fluid (see Table 1), the resulting wave impedance $\rho c/A_{\mathrm{ow}}$ would be approximately 470 GPa s/m^3 (equivalent to 233 dB in Fig. 2), exceeding experimental maximum values (Lynch et al., 1982). Additionally, Raufer et al. (2019) showed that the CP at the base behaves spring-like, a behavior not incorporated in the lumped element model.

The simulations presented in this paper help to reconcile these initially contradictory findings. The results depicted in Fig. 2 confirm that the cochlear fluid predominantly influences Z_{diff} at the lowest frequencies. However, the OSL at the cochlear base acts like a damped spring, shunting the inertial cochlear fluid above a resonance frequency, which is approximately 400 Hz in our model. At low and mid-frequencies, the OSL motion and the motion in the BM/CPB section are of similar magnitude [see Fig. 5(a)]. Due to its width being much larger than the widths of the CPB and BM in this region, the flexible OSL significantly contributes to the volume velocity flow between SV and ST (Raufer et al., 2019), causing a reduction of Z_{diff} compared to when considering the OSL as rigid. When the OSL contribution is missing, the fluid flow between SV and ST happens via the cochlear fluid moving along the CP, resulting in the inertial characteristic of Z_{diff} in these scenarios, reaching the magnitude of the fluid's wave impedance with rigid OSL and rigid CPB above 3 kHz.

Due to its impact on Z_{diff}, transitions observed in the radial motion profile of the OSL close to the base [Fig. 5(g)] result in a phase alternation of Z_{diff} around zero. Consequently, when averaged over individual curves (Frear et al., 2018), the characteristic of Z_{diff} becomes predominantly resistive. The contribution of the CPB to the volume velocity flow is minor, as indicated by the small differences between Z_{diff} with flexible and rigid CPB. Thus, it is mainly the motion of the OSL close to the base that is represented by the resistivity in the differential impedance.

4.1.2. RW impedance

The simulation results concerning the RW impedance Z_{rw} in Fig. 2 diverge above about 3 kHz between the conditions, even though Z_{rw} should, at first glance, remain unaffected by the CP motion. Upon examining the three-dimensional sound pressure data (not presented here), it became apparent that the OSL motion at the base and the modal break-up of the RW, as discussed by Stenfelt et al. (2004), result in a complex pressure distribution in the basal part of the ST, where

p_{st} is assessed. Since Z_{rw} is determined based on this sound pressure at a specific location, these effects elucidate the influence of the OSL's flexibility on Z_{rw}. Similar effects have been observed in terms of an increased variability of p_{st} with frequency (Nakajima et al., 2009), and a phase divergence between individually determined RW impedances towards higher frequencies (Frear et al., 2018). Consequently, it appears that some of the observed variability is more attributable to the determination method of Z_{rw} rather than being an inherent property of the impedance itself.

4.1.3. Cochlear input impedance

The cochlear input impedance [Fig. 2(c)], which characterizes the load of the stapes at the OW, shows only a slight influence by Z_{rw}, but is mostly dominated by Z_{diff}. Hence, the considerations regarding Z_{diff} are equally applicable to Z_c, suggesting a separation into different frequency ranges to be meaningful. Below about 400 Hz the primary load at the OW arises from the inertia of the cochlear fluid in SV and ST in conjunction with the compliance of the RW membrane. At higher frequencies, Z_c is predominated by the motion of the CP at the cochlear base, which exhibits resistive behavior on average.

Without considering the flexibility of the OSL and the CPB in cochlear models, the importance of the fluid might be overestimated, because it is not shunted by the moving OSL at the base. This omission could explain why the phase data of input impedances of cochlear models often indicates inertial effects, for example, in the models used in Gan et al. (2007) or Kim et al. (2014).

4.2. CP stiffness

Von Békésy (1960) conducted measurements of the CP compliance at nine positions along the CP of a human inner ear, revealing a change by a factor of about 100 between the base and the apex. However, cochlear models typically require a stiffness change of approximately 10 000 to obtain a frequency map on the BM which covers the frequency range of hearing (Naidu and Mountain, 1998). Fig. 3 provides an explanation which integrates both findings. With rigid OSL, our model reproduces the typical factor of more than four orders of magnitude between CP stiffness at the base and the apex. However, the simulations indicate that towards the base, CP stiffness is primarily influenced by the flexibility of the OSL, whereas towards the apex, it is influenced by the properties of the BM and CPB. Consequently, incorporating a flexible OSL led to variations in CP stiffness between the base and the apex, which align more closely with the experimentally determined values (von Békésy, 1960; Olson et al., 2012).

The results demonstrate that the CPB consistently contributes to the stiffness of the CP across all positions along the CP. Given that the widths of the CPB and the BM are approximately equal (Raufer et al., 2020), the CPB's influence on CP stiffness is primarily due to effectively increasing the width of the flexible BM/CPB section by nearly a factor of two compared to the BM alone.

In essence, these findings suggest that CP stiffness measurements reflect the combined stiffness of the BM, CPB, and OSL, rather than solely that of the BM. Moreover, upon inspection of the BM and differential velocity, these effects do not contradict the formation of a traveling wave along the CP. However, it is important to note that these findings may not apply to mammals with stiff OSL and without CPB, such as gerbils (Naidu and Mountain, 1998; Raufer et al., 2019). In these cases, reported discrepancies can be attributed to the measurement procedure involving point loading rather than pressure loading (Kapuria et al., 2017). Here, we applied pressure loading to determine CP stiffness, which more closely mimics the natural loading conditions of the cochlear fluid and better aligns with the experimental method used in the reference study of a human cochlea (von Békésy, 1960; Olson et al., 2012).

4.3. CP motion

4.3.1. Frequency dependence and traveling-wave characteristics

When normalized to the cochlear input, models typically predict a traveling wave behavior at fixed positions along the CP that is characterized by an increase in the magnitude of the BM velocity with a constant slope below the characteristic frequency, followed by a sharp decrease above it, and accompanied by a continuously decreasing phase (e.g., Zwislocki, 1950; Zweig et al., 1976; Kim et al., 2011; Wang et al., 2014; Ren et al., 2021). Similar curves were obtained with rigid OSL in Fig. 4(d)–(f).

However, experimental data from Gundersen et al. (1978) and Stenfelt et al. (2003), measured at 12 mm from the cochlear base, diverge from these classical predictions by exhibiting a frequency range with constant magnitude before reaching a maximum. Remarkably, our simulations replicate this behavior when the OSL is modeled as flexible [Fig. 4(e)]. A comparison between these velocity curves normalized to the cochlear input at the OW with those normalized to the differential cochlear pressure [Fig. 4(b)] and the differential impedance [Fig. 2(a)] reveals that this behavior arises from the interaction between the BM traveling-wave characteristics and the frequency-dependent properties of the differential impedance. Thus, these results highlight the need to consider differential impedance characteristics when analyzing BM motion as a transfer function relative to the input at the OW.

However, this differentiation is not commonly addressed in the literature, likely because classical models often assume there is no OSL motion, and studies on animals with stiff OSL have been widely used as experimental references (Raufer et al., 2019). While our results with a rigid OSL are consistent with those predictions, our findings with a flexible OSL underscore the significant role of the OSL's flexibility. This flexibility influences the relation between the differential cochlear pressure and the OW input, coupled through a damped, spring-like motion of the OSL rather than the inertial behavior of the cochlear fluid above a certain frequency (approximately 400 Hz in our model), as captured by the differential impedance Z_{diff}.

4.3.2. Position dependence

In addition to the frequency dependence, the CP's flexibility influences BM velocity in a position-dependent manner. The differential velocity analysis along the CP [Fig. 7(b)] suggests that the flexibility of the OSL and the presence of the CPB only slightly affect frequency mapping characteristics. Nevertheless, the boundary condition at the OSL–CPB junction for the traveling wave in the BM/CPB section varies from base to apex. Up to a relative distance of about 0.3, the stiffness at the BM center reflects the combined mechanical characteristics of the OSL (Fig. 3), resulting in OSL and BM motion of comparable magnitude in this region [Fig. 7(c)]. However, as the stiffness difference between the BM center and OSL–CPB junction increases towards the apex, the influence of the OSL's flexibility on the traveling wave characteristics diminishes.

Moreover, the velocity profiles in Fig. 5 demonstrate significant variability in CP motion along the radial direction, where even small positional differences on the BM and CPB can lead to magnitude changes of 5–10 dB at the cochlear base [cf. Raufer et al. (2019, Fig. 2)]. These differences can become even more pronounced at positions closer to the apex [Fig. 5 (g)–(i)].

4.3.3. Additional motion component and OSL traveling wave

Beyond the BM traveling wave's decay, the flexibility of the OSL introduces an additional motion component into the BM and CPB. This is evident from increased BM velocities with a flexible OSL compared to a rigid OSL in Fig. 4(c) and (e) and in the upper right parts of Fig. 6, as well as from similar radial magnitudes above the characteristic frequencies in Fig. 5(h) and (i). The decreasing phase at higher frequencies at the OSL–CPB junction for relative distances of 0.3 and 0.7 [Fig. 4(b) and (c)], suggests that this additional motion component

involves traveling-wave propagation in the OSL (Stenfelt et al., 2003). However, due to the OSL's layered structure and its decrease in width from base to apex (Raufer et al., 2020), the OSL traveling wave is less distinctly characterized than the BM traveling wave, which shows more clearly defined magnitude and phase patterns [Zweig et al. (1976); see Fig. 6(a) versus Fig. 7(a)]. Notable examples illustrating this complexity are the velocity increase across the OSL between 1–2 kHz at 0.7 relative distance [Fig. 5(f)], and its lever-like motion in response to a uniform load leading to non-meaningful stiffness values (Section 3.2). Thus, regarding the additional component of BM motion induced by the OSL, it may be more useful to conceptualize the OSL motion as a complex, frequency-dependent bending pattern in both radial (Fig. 5) and longitudinal directions [Fig. 7(a)], which is coupled to the BM motion through the CPB and via the cochlear fluid. Towards the apex, this motion component is further complicated by a radial break-up of the BM motion [Fig. 5(i) and (l)], which accounts for phase differences between the BM center and the OSL edge [Fig. 4(c)].

4.3.4. Role of the CPB

The flexibilities of both the OSL and the CPB contribute to an increase in phase lag in BM velocity, consistent with predictions by Taber and Steele (1981). However, the CPB's flexibility only contributes in terms of a slight increase in the magnitude of the BM motion compared to the OSL's flexibility, as indicated by the high similarity between BM velocity distributions with a rigid OSL [Fig. 6(b) and (c)]. Additionally, the radial velocity profiles underscore the CPB's role as a flexible connection between the OSL and BM (Raufer et al., 2019), an effect which varies little from base to apex.

4.3.5. Implications for interpreting CP motion

Further experimental data on CP motion is needed to improve its understanding, as our findings, in line with Raufer et al. (2019), partially diverge from the classical view on cochlear mechanics. Our results highlight the importance of considering the flexibility of the CP, particularly of the OSL, when interpreting CP velocity data, because this flexibility influences the differential pressure driving the traveling wave, alters the combined mechanical characteristics of the entire CP, and introduces additional BM motion through the OSL.

Furthermore, it is important to not interpret our simulated CP velocities and the reference data measured from temporal bone specimens (Gundersen et al., 1978; Stenfelt et al., 2003; Raufer et al., 2019) as equivalent to the input converted by inner hair cells into neural signals. While these investigations focussed on macro mechanics and linear passive mechanisms, in living ears, auditory nerve fibers show frequency tuning and active nonlinear mechanisms lead to an amplitude gain at the characteristic locations (Robles and Ruggero, 2001). These processes lead to a sharper tuning of auditory nerve responses compared to the BM velocity observed in passive models and dead specimens, where such active processes are absent. Notably, both the amplification by outer hair cells and the nerve response initiated by inner hair cells depend on the relative motion between the tectorial membrane and the hair cell stereocilia, which can be affected by the motion of the OSL and CPB (Raufer et al., 2019). At present, it remains unclear how the flexibility of the OSL influences both the transformation of BM motion into hair bundle displacement and the mechanisms behind cochlear amplification, particularly in terms of the level-dependent dynamics in BM versus OSL motion.

Moreover, when the sound pressure in the ear canal is used as a reference, rather than the OW volume velocity [Fig. 4(d)–(f)] or stapes velocity (Stenfelt et al., 2003), the middle ear transfer function introduces an additional frequency dependence, typically with a bandpass characteristic centered around 1 kHz (Koch et al., 2022). This frequency dependence would need to be added up to the characteristics observed in the CP motion in Fig. 4(d)–(f).

4.4. Study limitations and suggestions for future work

The material parameters utilized in our study were derived from experimental sources and other models to the extent possible (see Table 1). In cases where no references were available, reasonable values were assumed, leading to generally satisfactory agreements with experimental data in Section 3. We did not conduct a detailed parameter sensitivity analysis for the sake of brevity. Instead, focusing the simulations on a specific set of material parameters while varying between rigid and flexible OSL and CPB conditions helped to identify the mechanisms by which CP motion influences cochlear macromechanics. This understanding provides a basis for estimating the impact of influencing factors. For example, inter- or intraindividual variations in the Young's moduli of the vestibular and tympanic plates are expected to affect OSL stiffness (Fig. 3), with a proportional relationship at maximum, as approximated using the theory for sandwich structures (Zenkert, 1995). Such variations result in shifts in the resonances of the differential impedance [Fig. 2(a)], which scale with the square root of the stiffness. These resonance shifts, in turn, affect the characteristics of CP motion when normalized to the OW input [Fig. 4(d)–(f)].

The flexible OSL and the two windows were the only structures allowing fluid flow, while all other boundaries were considered rigid. However, it is important to note that fluid flow effects associated with small channels and other compliant structures in the inner ear have been demonstrated in other studies, e.g., in terms of leakage impedances (Frear et al., 2018). Similarly, the medial side of the OSL has been assigned with a fixed boundary condition within this study. Given that the modiolus consists of spongy bone encompassing the cochlear nerve and spiral ganglion, and that thin walls between different cochlear turns have been revealed by MicroCT scans (Bom Braga et al., 2023), additional flexibility and losses might be present through these boundaries in real ears. With an improved understanding of the role of the thin OSL structure achieved through this study, these structures could be explored in future investigations.

Furthermore, future models could integrate both linear/passive and nonlinear/active approaches (cf. mouse cochlea model by Motallebzadeh et al., 2018, Motallebzadeh and Puria, 2021) while incorporating the OSL as a flexible structure. In such models, it would be reasonable to distinguish between the structural damping and the viscous damping in the fluid, which were both captured by effective loss factors in our model. These studies could also enhance our understanding of the experimental variation related to these mechanisms, particularly in the cochlear impedances, by accounting for variations in inner ear shapes.

5. Conclusions

In this study, a finite element model of the human inner ear was employed to investigate how the flexibility of the CP, specifically the OSL and CPB, influences cochlear macro mechanisms by modeling these structures as either rigid or flexible. Our results underscore that the motion of the OSL close to the base plays a crucial role in the resistive behavior observed in both the differential impedance across the CP and the related cochlear input impedance. This, in turn, impacts the differential intracochlear sound pressure, which initiates a traveling wave propagation in the BM/CPB section along the flexible OSL. Above characteristic frequencies, an additional motion component enters the BM and CPB via the OSL. Radial velocity profiles highlighted frequency-dependent bending characteristics of the OSL towards the base, resulting in comparable magnitudes of BM and OSL motion at lower frequencies. Towards higher frequencies and closer to the apex, maximum magnitudes are reached in the BM/CPB section, aligning well with experimental measurements. Furthermore, the flexibility of the OSL was found to dominate the CP stiffness at the base relative to the stiffness of the BM itself, potentially elucidating discrepancies between model predictions and experimental data. The CPB consistently

contributes to stiffness and motion along the CP's length, effectively increasing the width of the flexible BM/CPB section compared to when considering the BM only.

In essence, our findings suggest that the flexibility of the OSL and the presence of the CPB significantly influence cochlear macro mechanisms. They emphasize the need for caution when interpreting CP motion based on classical models with rigid OSL and without CPB, highlighting the complexity introduced by these structures and the importance of additional experimental validation.

Source of funding

This work was funded by the Deutsche Forschungsgemeinschaft (DFG, German Research Foundation) – Project-ID 352015383 – SFB 1330 A4.

CRediT authorship contribution statement

Simon Kersten: Writing – original draft, Visualization, Methodology, Investigation, Formal analysis, Data curation, Conceptualization. **Henning Taschke:** Writing – review & editing, Methodology, Conceptualization. **Michael Vorländer:** Writing – review & editing, Supervision, Project administration, Funding acquisition, Conceptualization.

Declaration of competing interest

The authors declare that they have no known competing financial interests or personal relationships that could have appeared to influence the work reported in this paper.

Data availability

Research data for this article is available at https://doi.org/10.5281/zenodo.13897017. The repository contains the finite element model, simulation results, and a Python script with code used for the analysis.

Declaration of AI and AI-assisted technologies in the writing process

During the preparation of this work, the authors used ChatGPT 3.5 and 4.0, and Grammarly v0.24.0 to refine the English language and improve the wording of the manuscript. After using these tools, the authors reviewed and edited the content as needed, and take full responsibility for the content of the publication.

Appendix. CP coordinates

The CP coordinates (u_s and u_r) were derived numerically by solving a series of differential equations. Initially, the equation $\Delta u_s = 0$ was solved on the mutual edge of the BM/CPB boundary and the SL with boundary conditions $u_s = 0$ at the base and $u_s = 1$ at the apex, yielding a linear mapping along the longitudinal direction of the CP. This mapping was extended onto the BM/CPB boundary, into the OSL, and SL domain by sequentially solving $\Delta u_s = 0$ in each domain. The initial solution served as the boundary condition on the OSL edge, supplemented by a prescribed value of $u_s = 1$ at edges at the apex.

Radial coordinates u_r were determined along the BM/CPB boundary by solving $\Delta u_r = 0$, with boundary conditions set to $u_r = 0$ at the medial edge connected to the OSL and $u_r = 1$ at the lateral edge connected to the SL. The resulting coordinates are illustrated in Fig. A.8.

Local unit vectors of the CP coordinate system (r, s, and t) were defined to implement directional material properties (Fleischer et al., 2010). Here, s points longitudinally from base to apex, calculated as the normalized gradient of u_s, while t points perpendicularly from ST to SV. r points radially from OSL to SL, obtained as the cross product of s and t.

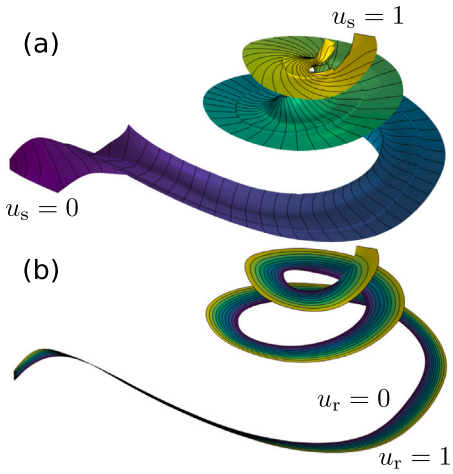

Fig. A.8. Illustration of longitudinal CP coordinates (u_s) from 0 (dark blue) at the base to 1 (yellow) at the apex (a), and radial coordinates (u_r) from 0 at the medial edge to 1 at the lateral edge of the BM/CPB boundary (b). Black contour lines represent distances of 0.01 (a) and 0.1 (b), respectively.

References

Agrawal, S., Schart-Morén, N., Liu, W., Ladak, H.M., Rask-Andersen, H., Li, H., 2018. The secondary spiral lamina and its relevance in cochlear implant surgery. Upsala J. Med. Sci. 123 (1), 9–18. http://dx.doi.org/10.1080/03009734.2018.1443983.

Aibara, R., Welsh, J.T., Puria, S., Goode, R.L., 2001. Human middle-ear sound transfer function and cochlear input impedance. Hear. Res. 152 (1), 100–109. http://dx.doi.org/10.1016/S0378-5955(00)00240-9.

Akhmanova, M., Osidak, E., Domogatsky, S., Rodin, S., Domogatskaya, A., 2015. Physical, spatial, and molecular aspects ofextracellular matrix of in vivo niches and artificial scaffolds relevant to stem cells research. Stem Cells Int. 2015, 167025. http://dx.doi.org/10.1155/2015/167025.

Anson, B., Donaldson, J., 1981. Surgical Anatomy of the Temporal Bone. W.B. Saunders company, Philadelphia, London, Toronto.

Atturo, F., Barbara, M., Rask-Andersen, H., 2014a. Is the human round window really round? An anatomic study with surgical implications. Otol. Neurotol. 35 (8), 1354. http://dx.doi.org/10.1097/MAO.0000000000000332.

Atturo, F., Barbara, M., Rask-Andersen, H., 2014b. On the anatomy of the 'hook' region of the human cochlea and how it relates to cochlear implantation. Audiol. Neurootol. 19 (6), 378–385. http://dx.doi.org/10.1159/000365585.

Auperrin, A., Delille, R., Lesueur, D., Bruyère, K., Masson, C., Drazétic, P., 2014. Geometrical and material parameters to assess the macroscopic mechanical behaviour of fresh cranial bone samples. J. Biomech. 47 (5), 1180–1185. http://dx.doi.org/10.1016/j.jbiomech.2013.10.060.

von Békésy, G., 1960. Experiments in Hearing. In: McGraw-Hill Series in Psychology, McGraw-Hill, New York.

Bhatt, K.A., Liberman, M.C., Nadol, J.B., 2001. Morphometric analysis of age-related changes in the human basilar membrane. Ann. Otol. Rhinol. Laryngol. 110 (12), 1147–1153. http://dx.doi.org/10.1177/000348940111001212.

Bom Braga, G.O., Parrilli, A., Zboray, R., Bulatović, M., Wagner, F., 2023. Quantitative evaluation of the 3D anatomy of the human osseous spiral lamina using MicroCT. J. Assoc. Res. Otolaryngol. 24 (4), 441–452. http://dx.doi.org/10.1007/s10162-023-00904-3.

Chang, Y., Kim, N., Stenfelt, S., 2016. The development of a whole-head human finite-element model for simulation of the transmission of bone-conducted sound. J. Acoust. Soc. Am. 140 (3), 1635–1651. http://dx.doi.org/10.1121/1.4962443.

Cohen, D., Blinder, G., Perez, R., Raveh, D., 2005. Standardized computed tomographic imaging and dimensions of the round-window niche. Int. Tinnitus J. 11 (2), 158–162.

Dallos, P., 1992. The active cochlea. J. Neurosci. 12 (12), 4575–4585. http://dx.doi.org/10.1523/JNEUROSCI.12-12-04575.1992.

De Paolis, A., Bikson, M., Nelson, J.T., de Ru, J.A., Packer, M., Cardoso, L., 2017. Analytical and numerical modeling of the hearing system: Advances towards the assessment of hearing damage. Hear. Res. 349, 111–128. http://dx.doi.org/10.1016/j.heares.2017.01.015.

Dobrev, I., Sim, J.H., 2018. Magnitude and phase of three-dimensional (3D) velocity vector: Application to measurement of cochlear promontory motion during bone conduction sound transmission. Hear. Res. 364, 96–103. http://dx.doi.org/10.1016/j.heares.2018.03.022.

Fleischer, M., Schmidt, R., Gummer, A., 2010. Compliance profiles derived from a three-dimensional finite-element model of the basilar membrane. J. Acoust. Soc. Am. 127 (5), 2973–2991. http://dx.doi.org/10.1121/1.3372752.

Frear, D.L., Guan, X., Stieger, C., Rosowski, J.J., Nakajima, H.H., 2018. Impedances of the inner and middle ear estimated from intracochlear sound pressures in normal human temporal bones. Hear. Res. 367, 17–31. http://dx.doi.org/10.1016/j.heares.2018.06.019.

Gan, R.Z., Reeves, B.P., Wang, X., 2007. Modeling of sound transmission from ear canal to cochlea. Ann. Biomed. Eng. 35 (12), 2180–2195. http://dx.doi.org/10.1007/s10439-007-9366-y.

Goycoolea, M.V., Lundman, L., 1997. Round window membrane. Structure function and permeability: A review. Microsc. Res. Tech. 36 (3), 201–211. http://dx.doi.org/10.1002/(SICI)1097-0029(19970201)36:3<201::AID-JEMT8>3.0.CO;2-R.

Gray, H., Lewis, W.H., 1918. Anatomy of the Human Body. Lea & Febiger.

Greenwood, D.D., 1990. A cochlear frequency-position function for several species—29 years later. J. Acoust. Soc. Am. 87 (6), 2592–2605. http://dx.doi.org/10.1121/1.399052.

Gundersen, T., Skarstein, ø., Sikkeland, T., 1978. A study of the vibration of the basilar membrane in human temporal bone preparations by the use of the mossbauer effect. Acta Oto-Laryngol. 86 (1–6), 225–232. http://dx.doi.org/10.3109/00016487809124740.

Heim, A.J., Matthews, W.G., Koob, T.J., 2006. Determination of the elastic modulus of native collagen fibrils via radial indentation. Appl. Phys. Lett. 89 (18), 181902. http://dx.doi.org/10.1063/1.2367660.

Kapuria, S., Steele, C., Puria, S., 2017. Unraveling the mystery of hearing in Gerbil and other rodents with an arch-beam model of the basilar membrane. Sci. Rep. 7 (1), http://dx.doi.org/10.1038/s41598-017-00114-x.

Kerkhofs, L., Starovoyt, A., Wouters, J., Putzeys, T., Verhaert, N., 2023. Optical coherence tomography-based atlas of the human cochlear hook region. J. Clin. Med. 12 (1), 238. http://dx.doi.org/10.3390/jcm12010238.

Kim, N., Homma, K., Puria, S., 2011. Inertial bone conduction: Symmetric and anti-symmetric components. J. Assoc. Res. Otolaryngol. 12 (3), 261–279. http://dx.doi.org/10.1007/s10162-011-0258-3.

Kim, N., Steele, C.R., Puria, S., 2014. The importance of the hook region of the cochlea for bone-conduction hearing. Biophys. J. 107 (1), 233–241. http://dx.doi.org/10.1016/j.bpj.2014.04.052.

Koch, M., Eßinger, T.M., Maier, H., Sim, J.H., Ren, L., Greene, N.T., Zahnert, T., Neudert, M., Bornitz, M., 2022. Methods and reference data for middle ear transfer functions. Sci. Rep. 12 (1), 17241. http://dx.doi.org/10.1038/s41598-022-21245-w.

Kohllöffel, L., 1983. Problems in aural sound conduction. In: de Boer, E., Viergever, M.A. (Eds.), Mechanics of Hearing: Proceedings of the IUTAM/ICA Symposium. Martinus Nijhoff ; Delft University Press, Delft, The Hague ; Boston, pp. 211–217.

Koike, T., Sakamoto, C., Sakashita, T., Hayashi, K., Kanzaki, S., Ogawa, K., 2012. Effects of a perilymphatic fistula on the passive vibration response of the basilar membrane. Hear. Res. 283 (1), 117–125. http://dx.doi.org/10.1016/j.heares.2011.10.006.

Li, P.M.M.C., Wang, H., Northrop, C., Merchant, S.N., Nadol, J.B., 2007. Anatomy of the round window and hook region of the cochlea with implications for cochlear implantation and other endocochlear surgical procedures. Otol Neurotol 28 (5), 641–648. http://dx.doi.org/10.1097/mao.0b013e3180577949.

Lim, J., Dobrev, I., Röösli, C., Stenfelt, S., Kim, N., 2022. Development of a finite element model of a human head including auditory periphery for understanding of bone-conducted hearing. Hear. Res. 421, http://dx.doi.org/10.1016/j.heares.2021.108337.

Liu, W., Atturo, F., Aldaya, R., Santi, P., Cureoglu, S., Obwegeser, S., Glueckert, R., Pfaller, K., Schrott-Fischer, A., Rask-Andersen, H., 2015. Macromolecular organization and fine structure of the human basilar membrane - RELEVANCE for cochlear implantation. Cell Tissue Res. 360 (2), 245–262. http://dx.doi.org/10.1007/s00441-014-2098-z.

Lynch, T.J., Nedzelnitsky, V., Peake, W.T., 1982. Input impedance of the cochlea in cat. J. Acoust. Soc. Am. 72 (1), 108–130. http://dx.doi.org/10.1121/1.387995.

Meenderink, S.W.F., Shera, C.A., Valero, M.D., Liberman, M.C., Abdala, C., 2019. Morphological immaturity of the neonatal organ of corti and associated structures in humans. J. Assoc. Res. Otolaryngol. 20 (5), 461–474. http://dx.doi.org/10.1007/s10162-019-00734-2.

Merchant, S.N., Ravicz, M.E., Rosowski, J.J., 1996. Acoustic input impedance of the stapes and cochlea in human temporal bones. Hear. Res. 97 (1), 30–45. http://dx.doi.org/10.1016/S0378-5955(96)80005-0.

Motallebzadeh, H., Puria, S., 2021. Mouse middle-ear forward and reverse acoustics. J. Acoust. Soc. Am. 149 (4), 2711–2731. http://dx.doi.org/10.1121/10.0004218.

Motallebzadeh, H., Soons, J.A.M., Puria, S., 2018. Cochlear amplification and tuning depend on the cellular arrangement within the organ of Corti. Proc. Natl. Acad. Sci. 115 (22), 5762–5767. http://dx.doi.org/10.1073/pnas.1720979115.

Naidu, R.C., Mountain, D.C., 1998. Measurements of the stiffness map challenge a basic tenet of cochlear theories. Hear. Res. 124 (1), 124–131. http://dx.doi.org/10.1016/S0378-5955(98)00133-6.

Nakajima, H.H., Dong, W., Olson, E.S., Merchant, S.N., Ravicz, M.E., Rosowski, J.J., 2009. Differential intracochlear sound pressure measurements in normal human temporal bones. J. Assoc. Res. Otolaryngol. 10 (1), 23–36. http://dx.doi.org/10.1007/s10162-008-0150-y.

Olson, E.S., 1998. Observing middle and inner ear mechanics with novel intracochlear pressure sensors. J. Acoust. Soc. Am. 103 (6), 3445–3463. http://dx.doi.org/10.1121/1.423083.

Olson, E.S., Duifhuis, H., Steele, C.R., 2012. Von Békésy and cochlear mechanics. Hear. Res. 293 (1), 31–43. http://dx.doi.org/10.1016/j.heares.2012.04.017.

Puria, S., 2003. Measurements of human middle ear forward and reverse acoustics: Implications for otoacoustic emissions. J. Acoust. Soc. Am. 113 (5), 2773–2789. http://dx.doi.org/10.1121/1.1564018.

Puria, S., Peake, W.T., Rosowski, J.J., 1997. Sound-pressure measurements in the cochlear vestibule of human-cadaver ears. J. Acoust. Soc. Am. 101 (5), 2754–2770. http://dx.doi.org/10.1121/1.418563.

Raufer, S., Guinan, J.J., Nakajima, H.H., 2019. Cochlear partition anatomy and motion in humans differ from the classic view of mammals. Proc. Natl. Acad. Sci. USA 116 (28), 13977–13982. http://dx.doi.org/10.1073/pnas.1900787116.

Raufer, S., Idoff, C., Zosuls, A., Marino, G., Blanke, N., Bigio, I.J., O'Malley, J.T., Burgess, B.J., Nadol, J.B., Guinan, J.J., Nakajima, H.H., 2020. Anatomy of the human osseous spiral lamina and cochlear partition bridge: Relevance for cochlear partition motion. J. Assoc. Res. Otolaryngol. 21 (2), 171–182. http://dx.doi.org/10.1007/s10162-020-00748-1.

Ren, L.J., Hua, C., Ding, G.H., Yang, L., Dai, P.D., Zhang, T.Y., 2018. Three-dimensional finite element hydrodynamical modeling of straight and spiral cochlea. AIP Conf. Proc. 1965 (1), 030003. http://dx.doi.org/10.1063/1.5038456.

Ren, L.-J., Yu, Y., Fang, Y.-Q., Hua, C., Dai, P.-D., Zhang, T.-Y., 2021. Finite element simulation of cochlear traveling wave under air and bone conduction hearing. Biomech. Model. Mechanobiol. 20 (4), 1251–1265. http://dx.doi.org/10.1007/s10237-021-01443-7.

Robles, L., Ruggero, M.A., 2001. Mechanics of the mammalian cochlea. Physiol. Rev. 81 (3), 1305–1352. http://dx.doi.org/10.1152/physrev.2001.81.3.1305.

Stenfelt, S., 2015. Inner ear contribution to bone conduction hearing in the human. Hear. Res. 329, 41–51. http://dx.doi.org/10.1016/j.heares.2014.12.003.

Stenfelt, S., Hato, N., Goode, R.L., 2004. Round window membrane motion with air conduction and bone conduction stimulation. Hear. Res. 198 (1), 10–24. http://dx.doi.org/10.1016/j.heares.2004.07.008.

Stenfelt, S., Puria, S., Hato, N., Goode, R.L., 2003. Basilar membrane and osseous spiral lamina motion in human cadavers with air and bone conduction stimuli. Hear. Res. 181 (1), 131–143. http://dx.doi.org/10.1016/S0378-5955(03)00183-7.

Taber, L.A., Steele, C.R., 1981. Cochlear model including three-dimensional fluid and four modes of partition flexibility. J. Acoust. Soc. Am. 70 (2), 426–436. http://dx.doi.org/10.1121/1.386785.

Taschke, H., 2005. Mechanismen Der Knochenschallleitung (Mechanisms of Bone-Conducted Sound) (Ph.D. thesis). Ruhr University Bochum, Bochum, Germany, http://dx.doi.org/10.13154/294-10197.

Wang, Y., Steele, C.R., Puria, S., 2016. Cochlear outer-hair-cell power generation and viscous fluid loss. Sci. Rep. 6 (1), 19475. http://dx.doi.org/10.1038/srep19475.

Wang, X., Wang, L., Zhou, J., Hu, Y., 2014. Finite element modelling of human auditory periphery including a feed-forward amplification of the cochlea. Comput. methods Biomech. Biomed. Eng. 17 (10), 1096–1107. http://dx.doi.org/10.1080/10255842.2012.737458.

Wright, C.G., Roland, P.S., 2018. Anatomy of the helicotrema and cochlear apex. In: Wright, C.G., Roland, P.S. (Eds.), Cochlear Anatomy Via Microdissection with Clinical Implications: an Atlas. Springer International Publishing, Cham, pp. 27–43. http://dx.doi.org/10.1007/978-3-319-71222-2_2.

Yang, L., van der Werf, K.O., Fitié, C.F.C., Bennink, M.L., Dijkstra, P.J., Feijen, J., 2008. Mechanical properties of native and cross-linked type I collagen fibrils. Biophys. J. 94 (6), 2204–2211. http://dx.doi.org/10.1529/biophysj.107.111013.

Zenkert, D., 1995. An Introduction to Sandwich Structures.

Zweig, G., Lipes, R., Pierce, J.R., 1976. The cochlear compromise. J. Acoust. Soc. Am. 59 (4), 975–982. http://dx.doi.org/10.1121/1.380956.

Zwislocki, J., 1950. Theory of the acoustical action of the cochlea. J. Acoust. Soc. Am. 22 (6), 778–784. http://dx.doi.org/10.1121/1.1906689.